phys. stat. sol. (b) **245**, No. 4, 623–640 (2008) / **DOI** 10.1002/pssb.200743359

physica status solidi b
www.pss-b.com
basic solid state physics

Feature Article

Calculating scattering matrices by wave function matching

M. Zwierzycki[*,1], P. A. Khomyakov[2], A. A. Starikov[2], K. Xia[3], M. Talanana[2], P. X. Xu[2], V. M. Karpan[2], I. Marushchenko[2], I. Turek[4], G. E. W. Bauer[5], G. Brocks[2], and P. J. Kelly[2]

[1] Institute of Molecular Physics, Polish Academy of Sciences, Smoluchowskiego 17, 60-179 Poznań, Poland
[2] Faculty of Science and Technology and MESA+ Institute for Nanotechnology, University of Twente, P.O. Box 217, 7500 AE Enschede, The Netherlands
[3] Beijing National Laboratory for Condensed Matter Physics, Institute of Physics, Chinese Academy of Sciences, Beijing 100080, P.R. China
[4] Institute of Physics of Materials, Academy of Sciences of the Czech Republic, 616 62 Brno, Czech Republic
[5] Kavli Institute of NanoScience, Delft University of Technology, Lorentzweg 1, 2628 CJ Delft, The Netherlands

Received 4 September 2007, revised 13 November 2007, accepted 26 November 2007
Published online 1 February 2008

PACS 71.15.–m, 72.10.Bg, 73.40.–c, 73.63.–b, 75.47.–m, 85.75.–d

[*] Corresponding author: e-mail Maciej.Zwierzycki@ifmpan.poznan.pl

The conductance of nanoscale structures can be conveniently related to their scattering properties expressed in terms of transmission and reflection coefficients. Wave function matching (WFM) is a transparent technique for calculating transmission and reflection matrices for any Hamiltonian that can be represented in tight-binding form. A first-principles Kohn–Sham Hamiltonian represented on a localized orbital basis or on a real space grid has such a form. WFM is based upon direct matching of the scattering-region wave function to the Bloch modes of ideal leads used to probe the scattering region. The purpose of this paper is to give a pedagogical introduction to WFM and present some illustrative examples of its use in practice. We briefly discuss WFM for calculating the conductance of atomic wires, using a real space grid implementation. A tight-binding muffin-tin orbital implementation very suitable for studying spin-dependent transport in layered magnetic materials is illustrated by looking at spin-dependent transmission through ideal and disordered interfaces.

1 Calculating the scattering matrix from first principles A recurring theme in condensed matter physics in the last twenty years has been the discovery of new physical effects and properties in systems with reduced dimensions. The prospect of exploiting these effects and properties in logical processing, sensing and storage devices is an important driving force behind nano-science and -technology. In semiconductors, the electronic structures of the electrons responsible for conduction can be described using simple models. The same is not true of the ferromagnetic (3d) transition metals which form the basis for magnetoelectronics and are characterized by multiply-sheeted Fermi surfaces with complicated topologies. A number of methods capable of describing complex electronic structures have been developed for calculating the conductance of multilayers, atomic wires and related structures from first principles [1–22], or using as input electronic structures which were calculated from first principles [23–29]. Most of them utilize the Green function expression for conductance first derived by Caroli [30] which reduces in the appropriate limit to the well known Fisher–Lee linear-response form [31] for the conductance of a finite disordered wire embedded between crystalline leads. An alternative linear-response technique, suitable for Hamiltonians that can be represented in tight-binding form, has been formulated by Ando [33] and is based upon direct matching of the scattering-region wave function to the Bloch modes of the leads. It can be shown to be fully equivalent to the Caroli expression [32]. A third approach based upon "embedding" [34, 35] has been combined with

full-potential linearized augmented plane wave method to yield what is probably the most accurate scheme to date [13, 14] but is numerically very demanding.

Our main purpose is to outline a scheme suitable for studying microscopic transport in the linear response regime in inhomogeneous materials which is (i) physically transparent and (ii) first-principles, i.e., requiring no free parameters. Landauer and Büttiker formulated the problem of electronic transport in terms of scattering matrices where the transmission matrix element $t_{m,n}$ is the probability amplitude that a state $|n\rangle$ in the left-hand lead incident on the scattering region from the left is scattered into a state $|m\rangle$ in the right-hand lead. The conductance $G = \mathrm{d}I/\mathrm{d}V|_{V=0}$ in the linear response regime is given by

$$G^{\mathrm{LB}} = \frac{e^2}{h} \sum_{n,m} |t_{m,n}|^2 = \mathrm{Tr}\,[\boldsymbol{t}\boldsymbol{t}^{\dagger}]\,. \tag{1}$$

The Landauer–Büttiker approach is intuitively very appealing because transport through nanostructures is so naturally described in terms of the scattering of electron waves that is transmission and reflection. Usually, explicit calculation of the scattering states is avoided by making use of the invariance properties of the trace in Eq. (1) to calculate the conductance directly from Green functions expressed in some convenient localized orbital representation [30]. However, we want to make contact with a large body of theoretical literature on mesoscopic physics [36, 37] which requires knowing the full microscopic transmission and reflection matrices and to make explicit use of the scattering states to analyze our numerical results. Our requirement of physical transparency is satisfied by choosing a computational scheme which yields the full scattering matrix and not just the conductance.

Any workable first-principles scheme is at present based upon an independent particle approximation. An extremely successful framework for calculating ground state properties of a wide variety of materials is Density Functional Theory (DFT) using functionals based upon the Local Density Approximation (LDA) or the Generalized Gradient Approximation (GGA). DFT/LDA or GGA calculations and their spin-polarized versions yield a charge (spin) density in all space as well as a Kohn–Sham effective potential. We assume that the latter can be used in describing the electron transport within the Landauer–Büttiker formalism in the linear response regime. This then satisfies our requirement of introducing no free parameters.

To calculate transmission and reflection matrices from first principles, we combined the wave-function matching (WFM) formalism described by Ando [33] for an empirical tight-binding Hamiltonian, with an ab-initio tight-binding Hamiltonian (or equation of motion in algebraically equivalent form). A version of this method has been implemented for a real-space grid using a high-order finite-difference scheme and applied to the calculation of the conductance of atomic wires [17, 38]. An implementation [8, 39] based upon an ab-initio TB-MTO basis [40] was applied to a number of problems of current interest in spin-transport: to the calculation of spin-dependent interface resistances where interface disorder was modeled by means of large lateral supercells [8, 41]; to calculating from first-principles the spin mixing conductance parameter [42] used to describe spin-transfer torque in systems with non-collinear magnetizations, and the Gilbert damping enhancement in the presence of interfaces [43]; to a generalized scattering formulation of the suppression of Andreev scattering at a ferromagnetic | superconducting interface [44]; to the problem of how spin-dependent interface resistances influence spin injection from a metallic ferromagnet into a III–V semiconductor [45–47]; to the influence of roughness and disorder on tunneling magnetoresistance [48]; to magnetization reversal by a spin-polarized heat current [49].

In this section we give a general exposé of the wave-function matching method. In Section 2 we discuss the application of a real-space grid implementation to atomic wires. Applications to layered (magnetic) structures based upon a TB-MTO implementation are discussed in Section 3.

1.1 Formalism The scattering problem is formulated for an infinite system consisting of the region of interest (an interface, junction, quantum wire etc.) sandwiched between two semi-infinite ideal leads. By replacing the semi-infinite leads by appropriate energy dependent boundary conditions, it can be reduced to finite size. This can be achieved by the wave-function matching (WFM) method for calculating the transmission and reflection matrices due to Ando [33]. In the next sections we will give a very sim-

First author Maciej Zwierzycki is a staff member at the Institute of Molecular Physics of the Polish Academy of Sciences in Poznan. He is primarily interested in the theory of spin-dependent transport phenomena in nanoscale structures such as magnetic multilayers, tunnel junctions, carbon nanotube devices etc. Using first-principles calculations, he investigates the relation between transport properties and the material's electronic structure.

ple, pedagogical introduction to this method, restricting ourselves to the linear response regime. The full details of the formalism and of the implementations can be found in [17, 32, 39].

1.1.1 Tight binding: Linear chain WFM can be formulated most naturally for tight-binding (TB) Hamiltonians. We illustrate it in one dimension for the atomic wire sketched in Fig. 1.

To keep matters simple we use an orthonormal basis consisting of a single atomic orbital per site. Furthermore we assume nearest neighbour interactions only. The diagonal elements of the Hamiltonian are $H_{i,i} = h_i$; its off-diagonal elements that are assumed real for simplicity, are $H_{i+1,i} = H_{i,i+1} = \beta_i$ and all elements $H_{j,i} = 0$ for $j > i+1$ and $j < i-1$ with i and j being site indices. The (Hermitian) Hamiltonian matrix is then

$$\boldsymbol{H} = \begin{pmatrix} \ddots & \cdots & 0 & 0 & \\ \vdots & h_{i-1} & \beta_{i-1} & 0 & 0 \\ 0 & \beta_{i-1} & h_i & \beta_i & 0 \\ 0 & 0 & \beta_i & h_{i+1} & \vdots \\ & 0 & 0 & \cdots & \ddots \end{pmatrix}. \tag{2}$$

The Schrödinger equation becomes[1]

$$(E\boldsymbol{I} - \boldsymbol{H})\,\psi = 0\,, \tag{3}$$

where ψ is the wave function represented by the column vector with the elements c_i describing the amplitude of the atomic orbital $|\chi_i\rangle$ on the i-th site. Written in its components, Eq. (3) has a form of infinite chain of equations

$$-\beta_{i-1}c_{i-1} + (E - h_i)\,c_i - \beta_i c_{i+1} = 0\,, \tag{4}$$

with i running from $-\infty$ to ∞.

We divide our system into three parts: a left lead, a scattering region, and a right lead. The left and right leads

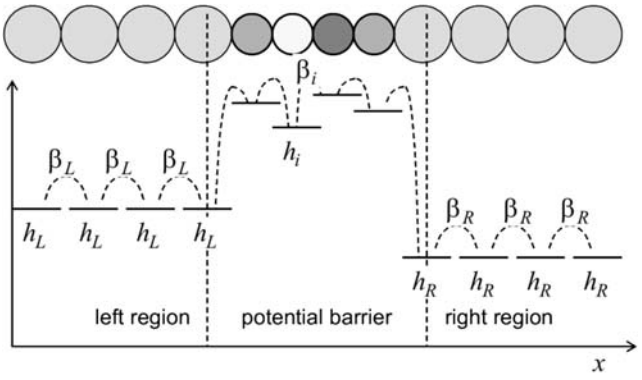

Figure 1 Nearest neighbor tight-binding model of an atomic chain. The periodic left and right regions are characterized by the on-site and hopping matrix elements $h_{\mathrm{L/R}}$ and $\beta_{\mathrm{L/R}}$. The scattering region has site dependent matrix elements h_i and β_i.

are crystalline materials with translational symmetry. Matrix elements in the leads must be site-independent, i.e. $h_i = h_{\mathrm{L/R}}$ and $\beta_i = \beta_{\mathrm{L/R}}$ for the left/right leads. Only in the scattering region do we have site-dependent matrix elements. The basic idea is illustrated in Fig. 1.

Ideal lead modes For sites i in the left (right) lead the matrix elements are site independent and Eq. (4) becomes

$$-\beta_{\mathrm{L(R)}}c_{i-1} + (E - h_{\mathrm{L(R)}})\,c_i - \beta_{\mathrm{L(R)}}c_{i+1} = 0\,. \tag{5}$$

As a consequence of the Bloch–Floquet theorem the wave functions in adjacent cells of a periodic system are related by a constant amplitude/phase factor λ, i.e.

$$\lambda c_{i-1} = c_i \quad \text{and} \quad \lambda c_i = c_{i+1}\,. \tag{6}$$

Combining Eqs. (5) and (6) yields the generalized linear eigenvalue problem for λ

$$\left[\begin{pmatrix} E-h & -\beta \\ 1 & 0 \end{pmatrix} - \lambda \begin{pmatrix} \beta & 0 \\ 0 & 1 \end{pmatrix}\right]\begin{pmatrix} c_i \\ c_{i-1} \end{pmatrix} = 0\,, \tag{7}$$

that has two solutions

$$-\beta + (E-h)\,\lambda - \beta\lambda^2 = 0$$

$$\Rightarrow \lambda_{\pm} = \frac{E-h}{2\beta} \pm \left[\left(\frac{E-h}{2\beta}\right)^2 - 1\right]^{1/2},$$

where the subscript L/R for the left and right leads has been omitted for simplicity. The roots λ can be expressed in a more familiar form. For $|(E-h)/2\beta| \le 1$ we define a wave number k by[2]

$$\cos(ka) = \frac{E-h}{2\beta}\,, \tag{8}$$

which leads to the simple form

$$\lambda_{\pm} = \mathrm{e}^{\pm ika}\,, \tag{9}$$

i.e. the familiar form of the Bloch factor, with λ_+ corresponding to a wave propagating to the right, and λ_- to a wave propagating to the left; a is the lattice constant of the ideal lead.

For $|(E-h)/2\beta| > 1$ one can define κ by

$$\cosh(\kappa a) = \left|\frac{E-h}{2\beta}\right|, \tag{10}$$

and obtain

$$\lambda_{\pm} = \begin{cases} +\mathrm{e}^{\mp\kappa a} & \text{if} \quad \dfrac{E-h}{2\beta} > 1\,; \\ -\mathrm{e}^{\mp\kappa a} & \text{if} \quad \dfrac{E-h}{2\beta} < -1\,. \end{cases} \tag{11}$$

[1] For non-orthogonal basis sets one introduces an overlap matrix $\boldsymbol{O}$, with matrix elements $O_{i,j} = \langle \chi_i \,|\, \chi_j \rangle$, and replaces $\boldsymbol{I}$ by $\boldsymbol{O}$.

[2] $E(k) = h + 2\beta\cos ka$ is of course the dispersion relation of a 1D s-band in the nearest neighbour tight-binding model.

Both these cases describe waves that decay either to the right or to the left, i.e. evanescent waves.[3] They are not acceptable as solutions of the Schrödinger equation for a translationally invariant system since they cannot be normalized. However they can play a role in a scattering problem, describing piecewise solutions, especially for three-dimensional structures.

Wave function matching Having obtained the modes of the ideal leads, we match them to the scattering region, where the matrix elements h_i and β_i in Eq. (4) are site dependent. We assume that the scattering region is localized in space, so i runs from 1 to N. For $i = 0$ Eq. (4) gives:

$$-\beta_{\mathrm{L}} c_{-1} + (E - h_0)\, c_0 - \beta_0 c_1 = 0\,, \tag{12}$$

where $h_0 = h_{\mathrm{L}}$. Assuming that the general solution in the left lead consists of the right- and left-going propagating modes, that is, incoming and reflected waves with amplitudes A and B, respectively, we can write the amplitude at the $i = -1$ site as

$$\begin{aligned} c_{-1} &= A\,\mathrm{e}^{ik(-a)} + B\,\mathrm{e}^{-ik(-a)} \equiv A\lambda_{\mathrm{L},+}^{-1} + B\lambda_{\mathrm{L},-}^{-1} \\ &= A\lambda_{\mathrm{L},+}^{-1} + (c_0 - A)\,\lambda_{\mathrm{L},-}^{-1}\,, \end{aligned} \tag{13}$$

where the last step follows because for $i = 0$ we have $c_0 = A + B$. In the scattering problem we assume that we have set the incoming wave so A is fixed. We can now use Eq. (13) to eliminate c_{-1} in Eq. (12), rewriting it as

$$(E - h_0 - \beta_{\mathrm{L}}\lambda_{\mathrm{L},-1}^{-1})\, c_0 - \beta_0 c_1 = A\beta_{\mathrm{L}}(\lambda_{\mathrm{L},+}^{-1} - \lambda_{\mathrm{L},-}^{-1})\,, \tag{14}$$

which truncates the infinite chain of Eq. (4) from the left. For $i = N + 1$, Eq. (4) gives:

$$-\beta_N c_N + (E - h_{N+1})\, c_{N+1} - \beta_{\mathrm{R}} c_{N+2} = 0\,, \tag{15}$$

where $h_{N+1} = h_{\mathrm{R}}$. In the right lead we assume there is only a transmitted, outgoing wave. Then, $c_{N+2} = c_{N+1}\lambda_{\mathrm{R},+}$,

$$-\beta_N c_N + (E - h_{N+1} - \beta_{\mathrm{R}}\lambda_{\mathrm{R},+})\, c_{N+1} = 0 \tag{16}$$

and the infinite chain of Eq. (4) from the right is also truncated. Using Eqs. (14) and (16), Eq. (3) can be replaced by

$$(E\boldsymbol{I} - \boldsymbol{H}')\,\psi = \boldsymbol{q}\,, \tag{17}$$

where ψ is a finite dimensional vector that contains the coefficients c_i in the scattering region plus those on the two boundary atoms, i.e. $i = 0, \ldots, N + 1$. $\boldsymbol{q}$ is a "source" vector of length $N + 2$, whose coefficients are zero, except for the first one which is

$$q_0 = A\beta_{\mathrm{L}}(\lambda_{\mathrm{L},+}^{-1} - \lambda_{\mathrm{L},-}^{-1})\,. \tag{18}$$

$\boldsymbol{H}'$ is a finite $(N + 2) \times (N + 2)$ Hamiltonian matrix. All its matrix elements are identical to those of the original Hamiltonian matrix, Eq. (2), except for the first and the last diagonal elements, which are

$$H'_{0,0} = h_0 + \Sigma_{\mathrm{L}}(E), \qquad H'_{N+1,N+1} = h_{N+1} + \Sigma_{\mathrm{R}}(E)\,, \tag{19}$$

with

$$\Sigma_{\mathrm{L}}(E) = \beta_{\mathrm{L}}\lambda_{\mathrm{L},-}^{-1} \quad \text{and} \quad \Sigma_{\mathrm{R}}(E) = \beta_{\mathrm{R}}\lambda_{\mathrm{R},+}\,. \tag{20}$$

In Green function jargon $\Sigma_{\mathrm{L/R}}(E)$ are called the self-energies of the left and right leads. They contain all the information concerning the coupling of the scattering region to the leads. The self-energies are complex and energy dependent through Eqs. (8) and (9).

We have replaced an infinite dimensional problem, Eq. (3), by a finite dimensional one, Eq. (17). Once Eq. (17) is solved, all that remains is to extract the transmission coefficient given by the amplitude of the wave function in the right lead normalized to the amplitude of the incoming wave, and (flux) normalized with velocities to obtain the unitary scattering matrix [32, 33]

$$t = \sqrt{\frac{v_{\mathrm{R}}/a_{\mathrm{R}}}{v_{\mathrm{L}}/a_{\mathrm{L}}}}\,\frac{c_{N+1}}{A}\,, \tag{21}$$

with the velocities given by

$$v = -\frac{2\beta a}{\hbar}\sin(ka)\,. \tag{22}$$

The source term (18) then reduces to

$$q_0 = \frac{i\hbar A}{a_{\mathrm{L}}}\,v_{\mathrm{L}}\,. \tag{23}$$

From Eqs. (20) and (22) we can relate the velocities to the self-energies

$$v_{\mathrm{L/R}} = -\frac{2a_{\mathrm{L/R}}}{\hbar}\,\mathrm{Im}\,\Sigma_{\mathrm{L/R}}(E)\,. \tag{24}$$

Using WFM, simple scattering problems with tight-binding Hamiltonians can be solved analytically in a straightforward way, as illustrated in [32, 38].

Green function expressions These results can be put into a very compact form using Green functions. One can define a Green function matrix ("Green matrix") by

$$\boldsymbol{G}(E) = (E\boldsymbol{I} - \boldsymbol{H}')^{-1}\,. \tag{25}$$

Like the modified Hamiltonian matrix $\boldsymbol{H}'$, it has dimensions $N + 2$. One can also define the infinite dimensional retarded Green matrix related to the original infinite dimensional Hamiltonian

$$\boldsymbol{G}^{\mathrm{r}}(E) = [(E + i\eta)\,\boldsymbol{I} - \boldsymbol{H}]^{-1}\,, \tag{26}$$

where η is a real, positive infinitesimal. For z a complex number in the upper half plane, the matrix elements of $\boldsymbol{G}(z)$ and $\boldsymbol{G}^{\mathrm{r}}(z)$ in the scattering region are identical [50]. Note that $\boldsymbol{H}'$ is non-Hermitian, because the self-energy Σ is complex, see Eqs. (19) and (20). One can show that the

[3] We label right- and left-decaying solutions as right- and left-going modes respectively.

eigenvalues of $\boldsymbol{H}'$ that correspond to the continuous spectrum of Eq. (3), are not real and lie in the upper half complex plane. Thus $\boldsymbol{G}(E)$ is a well-defined quantity for real energies E.[4] By construction it has the retarded boundary condition build into it and one does not need the usual $+i\eta$ trick.

The definition of $\boldsymbol{G}$ allows us to write

$$c_{N+1} = G_{N+1,0}(E)\, q_0 \,, \tag{27}$$

see Eq. (17). Equations (21), (23) and (27) then lead to a compact Fisher–Lee expression [31] for the transmission amplitude

$$t = i\hbar \sqrt{\frac{v_{\mathrm{R}} v_{\mathrm{L}}}{a_{\mathrm{R}} a_{\mathrm{L}}}}\; G_{N+1,0}(E)\,, \tag{28}$$

which relates matrix elements of the scattering matrix to elements of the Green matrix. Using Eq. (24) we can write

$$t = i \sqrt{-2\,\mathrm{Im}\,\Sigma_{\mathrm{R}}}\; G_{N+1,0}(E) \sqrt{-2\,\mathrm{Im}\,\Sigma_{\mathrm{L}}}\,, \tag{29}$$

which allows the transmission probability to be written as

$$T = t^{*}t = \Gamma_{\mathrm{R}} G^{\mathrm{r}}_{N+1,0} \Gamma_{\mathrm{L}} G^{\mathrm{a}}_{0,N+1}\,, \tag{30}$$

with all quantities evaluated at a fixed energy E. $\boldsymbol{G}^{\mathrm{a}} = [\boldsymbol{G}^{\mathrm{r}}]^{\dagger}$ is the advanced Green matrix and $\Gamma_{\mathrm{L/R}} = -2\,\mathrm{Im}\,\Sigma_{\mathrm{L/R}}$. Equation (30) is known as the Caroli expression [30].

1.1.2 Wave function matching in three dimensions The ideas of the previous section can be straightforwardly extended to a three dimensional system described by a TB Hamiltonian, provided it can be partitioned into a set of principal layers (PL) defined so that hopping only exists between neighbouring layers. The h_i and β_i are then substituted by matrices of dimension H equal to the total number of atomic orbitals within the principal layer. The method can be formulated equally well for systems with finite cross-section (i.e. wires) and for layered systems that are periodic along the interfaces. In the latter case, blocks of the Hamiltonian will be indexed by $\boldsymbol{k}_{\parallel}$. The equivalent of the lead problem (7) must be then solved numerically and yields a set of $2H$ solutions divided into equal numbers of left- and right- going states. In general there are both propagating and evanescent modes present at any given energy. While only the former modes need to be taken into account in the Landauer–Büttiker formula (1), it is essential that the full set of modes be retained in the matching procedure.

Most of the Green function expressions we obtained in the one-dimensional case can be generalized to three dimensions. In particular, it is possible to explicitly demonstrate the equivalence of the WFM approach coupled with the Landauer–Büttiker formula, and the Caroli expression [32].

[4] We notice that $\boldsymbol{G}(E)$ might have poles for a discrete set of real energies that correspond to the localized states of Eq. (3). However, the localized states do not contribute to the physical transmission Eq. (28).

WFM can be applied to any equation of motion with the algebraic structure of a block-tridiagonal TB Hamiltonian. Examples include the Schrödinger equation discretized on a real-space grid [17, 32] or the KKR (tail cancellation) equation in a tight-binding representation [8, 39]. These are discussed in the following section together with illustrative applications.

2 Real space grid implementation: Conductance of atomic wires Application of the WFM technique for solving the scattering problem relies on a real space representation of the Kohn–Sham Hamiltonian and the wave functions. An efficient implementation based upon a high-order finite-difference scheme is discussed in [17]. In general, finite-difference schemes are suitable for treating systems with little symmetry and have a computational efficiency that is comparable to that of plane wave basis set representations [51–54].

We can write the Kohn–Sham equation in a form that is similar to Eq. (4), by putting the wave function ψ and the Kohn–Sham one-electron potential V on an equidistant grid in real space $\boldsymbol{r} = (x_j, y_k, z_l)$, where $x_j = x_0 + jh_x$, $y_k = y_0 + kh_y$, $z_l = z_0 + lh_z$ and h_x, h_y, h_z are the grid spacings in the x,y- and z-directions, respectively. It is computationally advantageous to approximate the second derivative in the Kohn–Sham equation using a high-order finite-difference scheme [17]. For the x part this yields

$$\frac{\partial^2 \psi(x_j, y_k, z_l)}{\partial x^2} \approx \frac{1}{h_x^2} \sum_{n=-N}^{N} c_n \psi(x_{j+n}, y_k, z_l)\,, \tag{31}$$

with similar expressions for the y and z parts. Expressions for the coefficients c_n for various values of N are tabulated in [52]. The simplest approximation, $N = 1$ (where $c_1 = c_{-1} = 1$ and $c_0 = -2$) reduces Eq. (31) to the textbook finite-difference expression for the second derivative. However, in [17] it is demonstrated that the scattering problem can be solved much more efficiently using high-order finite-difference approximations with $N = 4-6$.

In a finite-difference approximation the Kohn–Sham equation becomes

$$\begin{aligned}(E - V_{j,k,l})\,\psi_{j,k,l} + \sum_{n=-N}^{N} (t_n^{x} \psi_{j+n,k,l} + t_n^{y} \psi_{j,k+n,l} \\ + t_n^{z} \psi_{j,k,l+n}) = 0\,,\end{aligned} \tag{32}$$

where $V_{j,k,l}\psi_{j,k,l}$ is a shorthand notation for $V(x_j, y_k, z_l)\,\psi(x_j, y_k, z_l)$ and $t_n^{x,y,z} = \hbar^2/2mh_{x,y,z}^2 \times c_n$. In order to make a connection to the formalism explained in the previous section, we divide the wire into cells of dimension $a_x \times a_y \times a_z$. The direction of the wire is given by the x-axis. The number of grid points in a cell is $L = a_x/h_x$, $W_y = a_y/h_y$, $W_z = a_z/h_z$ for the x,y- and z-directions respectively. The values $\psi_{j,k,l}$ where the indices j, k, l correspond to a single cell i are grouped into a supervector $\boldsymbol{\Psi}_i$. The idea is shown in Fig. 2. This supervector has the di-

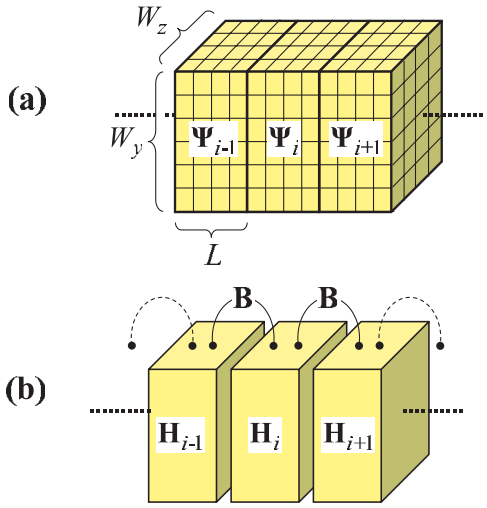

Figure 2 (online colour at: www.pss-b.com) (a) System is divided into cells labelled by an index i. The cells contain L, W_y and W_z grid points in the x,y- and z-directions, respectively. $\boldsymbol{\Psi}_i$ is the supervector that contains the wave function values on all grid points in cell i. (b) $\boldsymbol{H}_i$ is the Hamilton matrix connecting grid points within cell i; the $\boldsymbol{B}$-matrix connects grid points between neighboring cells and is independent of i for ideal leads.

mension $N_{\mathrm{rs}} = L \cdot W_y \cdot W_z$, which is the total number of real space grid points in a cell. If we let i denote the position of the cell along the wire then Eq. (32) can be rewritten as

$$-\boldsymbol{B}\boldsymbol{\Psi}_{i-1} + (E\boldsymbol{I} - \boldsymbol{H}_i)\,\boldsymbol{\Psi}_i - \boldsymbol{B}^{\dagger}\boldsymbol{\Psi}_{i+1} = 0\,, \tag{33}$$

for $i = -\infty, \ldots, \infty$. Here $\boldsymbol{I}$ is the $N_{\mathrm{rs}} \times N_{\mathrm{rs}}$ identity matrix.

The matrix elements of the $N_{\mathrm{rs}} \times N_{\mathrm{rs}}$ matrices $\boldsymbol{H}_i$ and $\boldsymbol{B}$ can be derived straightforwardly from Eq. (32). The expressions are given in [17]. Clearly Eq. (33) is similar to Eq. (4), which means that we can use the WFM method to solve the scattering problem.

As a first step, the one-electron self-consistent potentials of the bulk leads and the scattering region containing the wire are obtained from DFT calculations. Subsequently the scattering problem is solved at the Fermi energy by matching the modes in the leads to the wave function in the scattering region.

2.1 Conductance of monatomic sodium wires

Conductors whose cross section contains only a small number of atoms are commonly called "atomic wires". Clear evidence that the fundamental limit of a one atom cross section can be reached has been presented for gold atomic wires [55, 56]. Over the last decade the electronic transport in atomic wires made of various metals has been characterized in great detail experimentally [57–59]. Such wires have conductances of the order of the quantum unit $G_0 = 2e^2/h$.[5] Atomic wires that have a cross section of just one atom, so-called "monatomic" wires, are the ultimate examples of quasi-one-dimensional systems. Here the effects of a reduced dimensionality are expected to be most pronounced. One of the most striking features of monatomic wires is the non-monotonic behavior of the conductance as a function of the number of atoms in the wire [60, 61]. Specifically, the conductance in such wires oscillates. For simple monovalent metals the oscillation has a period that corresponds to two atoms, i.e. the conductance of wires consisting of an odd number of atoms is different from that of even numbered wires. The amplitude of such oscillations is of order 0.1 G_0. The central questions are: what determines the phase and amplitude of the oscillation and how robust are these with respect to changes in the geometry of the wire and in the coupling between the wire and the leads?

From our first-principles calculations on sodium monatomic wires we find that odd numbered wires always have a conductance close to 1 G_0 and that this value is not very sensitive to changes in the geometry or in the coupling [38]. Even numbered wires have lower conductances, whose values are determined by the geometry and the coupling. This general pattern can be understood from the electronic levels of free-standing wires giving rise to transmission resonances. We analyze our first-principles results using a simple tight-binding model. In particular, we show that local charge neutrality of the sodium wires provides a strong constraint on the phase of the conductance oscillation. In the absence of a significant charge transfer between the wire and the leads, a transmission resonance is pinned at the Fermi energy for wires containing an odd number of atoms, which leads to a conductance close to one quantum unit. Obtaining quantitative values for the conductance, of even-numbered wires in particular, requires well-converged first-principles calculations using a realistic structure of the wire and the leads.

The one-electron potentials of the leads and the scattering regions are extracted from two self-consistent DFT calculations for bulk bcc sodium and for the supercell shown in Fig. 3, respectively, using a standard approach based upon normconserving pseudopotentials and a plane wave basis set. It turns out that, in order to obtain potentials that are converged, the total energies in such self-consistent calculations have to be converged to within 5×10^{-7} Hartrees. One assumes that the leads outside the scattering region consist of bulk material. This means that at the edges of the scattering region, the potential should join smoothly to the potentials of the bulk leads. We have checked that this is the case. Enlarging the scattering region by including two extra atomic layers in each lead changes the results reported for the conductance only by ~1.5% for even-numbered wires and 0.5% for odd-numbered wires. The Fermi energy is extracted from the bulk calculation [17]. The only parameters in calculating the conductance within the finite-difference scheme are the order N of the finite-difference approximation of the kinetic energy (i.e., the second derivative) and the spacing $h_{x,y,z}$ between the real-space grid points. We use $N = 4$ and

[5] The factor of 2 with respect to Eq. (1) results from spin degeneracy.

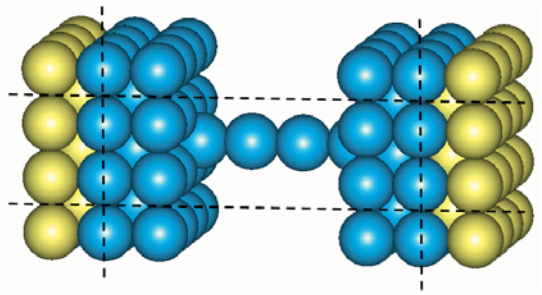

Figure 3 (online colour at: www.pss-b.com) Structure of an atomic wire consisting of two sodium atoms between two sodium leads terminated by (001) surfaces. The boundaries of the supercell are indicated by dashed lines. Bulk atoms are indicated by yellow (light grey) balls and atoms in the scattering region by blue (dark grey) balls, respectively.

$h_{x,y,z} = 0.80a_0$ (a_0 being the = Bohr radius); for details and convergence tests we refer to [17]. The total transmission is averaged over an 8×8 $\boldsymbol{k}_{\|}$-point grid in the lateral BZ of the supercell. Most calculations are done for a 2×2 lateral supercell. Enlarging the supercell changes the conductance only marginally as discussed in [38].

The electron transport in the crystalline leads is ballistic, i.e. an electron goes through the leads without any scattering. The transport properties of a monatomic wire suspended between two leads depend upon three factors; the number of atoms in the chain, the geometry of the wire, and the contact between wire and leads.

The calculated conductance as a function of the number of atoms in the atomic chain is given in Fig. 4. Since a sodium atom has valence one, both the infinite sodium chain and bulk sodium have a half-filled band, and the infinite wire has one conducting channel at the Fermi level. The conductance of the infinite chain is equal to the quantum unit G_0, and the conductance of finite wires is $\leq G_0$. As can be observed in Fig. 4 the conductance exhibits a regular oscillation as a function of the number of atoms in the wire. The conductance is very close to G_0 for odd-numbered wires, and for even-numbered wires it is ~10% lower. Such a behavior of the conductance in atomic-sized conductors is very different from ohmic behavior in macroscopic conductors; it expresses the quantum nature of the electron transport at the nanoscale.

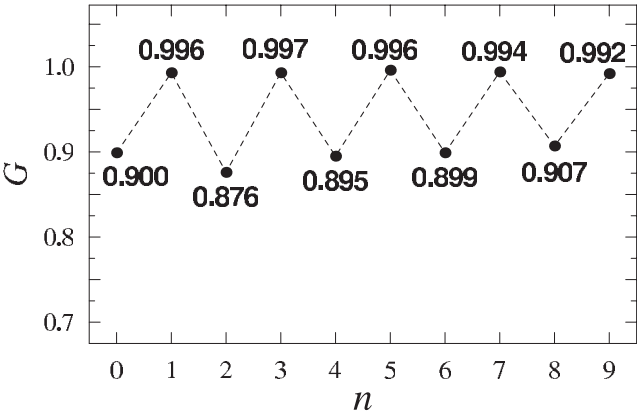

Figure 4 Conductance (in units of G_0) as a function of the number of atoms in the atomic chain. All atomic bond lengths in the system are equal to the bulk value $d = 6.91a_0$.

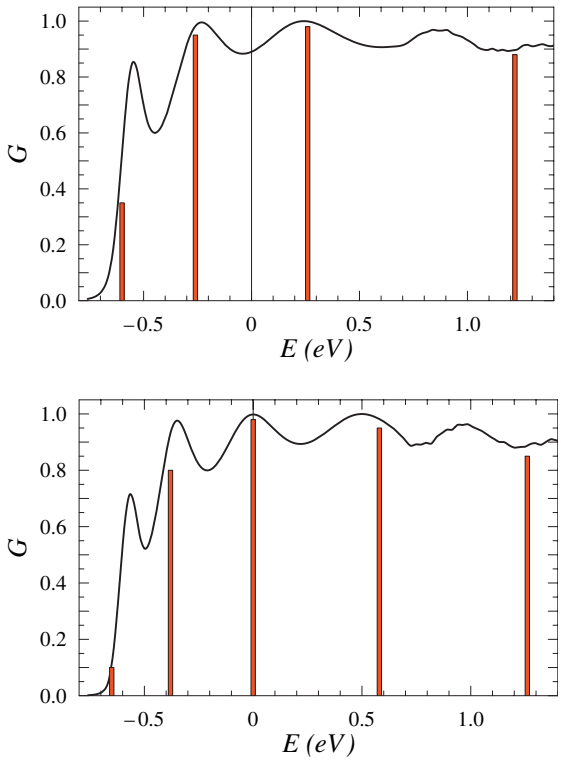

Figure 5 (online colour at: www.pss-b.com) Conductance (in units of G_0) as a function of energy for monatomic wires consisting of four (top figure) and five (bottom figure) atoms. The red (grey) bars correspond to the energy levels of free-standing wires. $E = 0$ corresponds to the Fermi level.

In order to interpret the even-odd oscillation we have calculated the conductance as a function of energy for wires of different length. The results for monatomic wires consisting of four and five atoms are shown in Fig. 5. Resonant peaks in the conductance can be clearly identified. Qualitatively they correspond to energy levels of a free-standing Na wire which are shifted and broadened into resonances by the interaction of the wire with the leads. To illustrate this, the calculated energy levels of free-standing wires of four and five atoms are shown as bars in Fig. 5. The levels are sufficiently close to the resonant energies to warrant an interpretation of the conductance in terms of a transmission through levels of the wire. As is clearly observed in Fig. 5, the Fermi level is in between two resonant peaks for a four atom wire and right on top of a resonance for a five atom wire. By calculating the conductance as a function of energy for wires of different length it can be shown that this observation can be generalized. The Fermi

level is between resonances for even-numbered wires and on top of a resonance for odd-numbered wires.

2.1.1 Simple tight-binding model To support the intuitive picture presented in the previous section we use a simple tight-binding model as shown in Fig. 1, in which the leads are modeled as quasi-one-dimensional systems described by effective parameters. Here $h_L = h_R = \varepsilon_0$ and $\beta_L = \beta_R = \beta$ are, respectively, the on-site energies and nearest neighbour hopping coefficients of the leads while $h_i = \varepsilon_0'$ and $\beta_i = \beta'$ are the corresponding wire parameters. The coupling between the left (right) electrode and the atomic chain is given by the hopping coefficient β_c (β_c').

If the system has mirror symmetry, the coupling is symmetric, i.e. $\beta_c = \beta_c'$. The leads and the chain are made of the same material (sodium). If one assumes that all atoms are neutral (local charge neutrality), then it is not unreasonable to set $\varepsilon_0 = \varepsilon_0'$. The conductance can be calculated analytically for this model using WFM [32]. The parameter β can be used as a scaling parameter. In the following all energy parameters $\varepsilon_0, \varepsilon_0', \beta', \beta_c, \beta_c'$ are in units of β. At the Fermi energy, the conductance of a wire consisting of n atoms is given by

$$G = \begin{cases} G_0 & \text{if} \quad n \text{ is odd}; \\ G_0 \dfrac{4\beta_c^4/\beta'^2}{[1+\beta_c^4/\beta'^2]^2} & \text{if} \quad n \text{ is even}. \end{cases} \tag{34}$$

The conductance for odd-numbered wires is equal to the quantum unit, and it is smaller than the quantum unit for even-numbered wires (unless by accident $\beta_c^2 = \beta'$).

It is instructive to study some other consequences of the tight-binding model. If $\Delta\varepsilon = \varepsilon_0 - \varepsilon_0' \neq 0$ then a charge transfer will take place between the leads and the wire. The conductance calculated at the Fermi energy for a one-site wire ($n = 1$) and a two-site wire ($n = 2$) becomes, respectively,

$$G = G_0 \frac{4\beta_c^4}{\Delta\varepsilon^2 + 4\beta_c^4}, \tag{35}$$

$$G = G_0 \frac{4\beta_c^4\beta'^2}{[\beta_c^4 + (\beta' + \Delta\varepsilon)^2][\beta_c^4 + (\beta' - \Delta\varepsilon)^2]}. \tag{36}$$

According to Eq. (35), a nonzero $\Delta\varepsilon$ suppresses the transmission through a one-site wire. The transmission is shifted "off resonance" and the conductance becomes smaller than the quantum unit. However, the coupling between wire and lead also causes a broadening of the resonance, which is proportional to β_c. This broadening partially compensates for the decrease of the conductance. If the coupling is sufficiently strong, i.e. $4\beta_c^4 \gg \Delta\varepsilon^2$, then the conductance is again close to the quantum unit. In the limit of weak coupling, i.e. $4\beta_c^4 \ll \Delta\varepsilon^2$, the conductance goes to zero with decreasing β_c for any nonzero $\Delta\varepsilon$.

The conductance of a two-site wire, see Eq. (36), behaves qualitatively differently as a function of the coupling strength β_c. In the weak coupling limit, i.e. $\beta_c^4 \ll (\beta' \pm \Delta\varepsilon)^2$ the conductance goes to zero with decreasing β_c and the decrease is faster than for a one-site wire. Note that this only holds for $\Delta\varepsilon \ll \beta'$. If $\Delta\varepsilon \sim \beta'$ then the conductance decreases more slowly with decreasing β_c for a two-site wire than for a one-site wire.[6]

If the coupling between wire and lead is strong, i.e. $\beta_c^4 \gg (\beta' \pm \Delta\varepsilon)^2$, then the conductance always decreases with increasing β_c. This is due to a phenomenon called "pair annihilation" of resonances [62], which happens if the resonance widths become larger than the spacing between the resonances. Between the strong and weak coupling regimes there is a value of β_c (close to 1) where the conductance of a two-site wire is equal to the quantum unit.

The conductance of longer wires, i.e. $n > 2$, can be interpreted along the same lines. For small $\Delta\varepsilon$, the odd-numbered wires resemble the one-site wire and the even-numbered wires resemble the two-site wire. For a very large range of coupling strengths β_c one obtains an even-odd oscillation in the conductance of a nearly constant amplitude. The conductance of odd-numbered chains is close to the quantum unit and that of even-numbered chains is smaller by an amount that depends upon the coupling between wire and lead. Apparently, this is the case that corresponds to the results of our first-principles calculations, see Fig. 4. If $\Delta\varepsilon$ becomes larger, the conductance of all wires as a function of β_c becomes qualitatively similar to that of the two-site wire. The amplitude and even the phase of the conductance oscillation as a function of the wire length then strongly depends upon the coupling β_c of the wire to the lead. Note that if $\Delta\varepsilon$ is significant, it will be accompanied by a significant charge transfer between wire and leads. In our first-principles calculations we have found no indication of such a large charge transfer.

In conclusion, odd-numbered wires have a conductance close to the quantum unit $G_0 = 2e^2/h$ and even-numbered wires have a lower conductance. This oscillation is remarkably robust, as we show by systematically varying the structure of the wires and the geometry of the contacts between the wires and the electrodes. The phase of the oscillation is not affected by these structural variations. The conductance of even-numbered wires is sensitive to the wire geometry. Increasing the interatomic distances in the wire and/or strengthening the contacts between wire and leads increases the conductance of even-numbered wires; increasing the asymmetry between the interatomic distances or between left and right contacts decreases the conductance.

3 TB-MTO implementation: Layered (magnetic) structures Magnetoelectronic devices such as magnetic multilayers usually contain layers of ferromagnetic transi-

[6] This holds true except for $\Delta\varepsilon = \pm\beta'$ when the conductance increases with decreasing β_c and approaches G_0 for $\beta_c \ll 4\beta'^2$.

tion metals. The magnetism of these metals is related to the presence in their electronic structures of open shells of itinerant 3d electrons. These form narrow bands and hybridize with strongly delocalized s-electrons. The resulting band structures are complicated, often with multiple bands crossing the Fermi level, and can not be described by simple models. The appropriate framework for treating itinerant electron systems from first-principles is the Local Spin-Density Approximation (LSDA) of Density Functional Theory(DFT) [63].

Oscillatory exchange coupling in layered magnetic structures was discussed by Bruno in terms of generalized reflection and transmission matrices [64] which were calculated by Stiles [65, 66] for realistic electronic structures using a scheme [1, 2] based on linearized augmented plane waves (LAPWs). At an interface between a non-magnetic and a magnetic metal, the different electronic structures of the majority and minority spin electrons in the magnetic material give rise to strongly spin-dependent reflection [67, 68]. Schep et al. used transmission and reflection matrices calculated from first-principles with an embedding surface Green function method [69] to calculate spin-dependent interface resistances for specular Cu | Co interfaces embedded in diffusive bulk material [4]. The resulting good agreement with experiment indicated that interface disorder is less important than the spin-dependent reflection and transmission from a perfect interface. Calculations of domain wall resistances as a function of the domain wall thickness illustrated the usefulness of calculating the full scattering matrix [5, 70]. However, the LAPW basis set used by Stiles and Schep is computationally too expensive to allow repeated lateral supercells to be used to model interfaces between materials with very different, incommensurate lattice parameters or to model disorder. This is true of all plane-wave based basis sets which typically require of order 100 plane waves per atom in order to describe transition metal atom electronic structures reasonably well.

Muffin-tin orbitals (MTO) form a flexible, minimal basis set leading to highly efficient computational schemes for solving the Kohn-Sham equations of DFT [71, 72, 40]. For the close packed structures adopted by the magnetic materials Fe, Co, Ni and their alloys, a basis set of 9 functions (s-, p- and d-orbitals) per atom in combination with the atomic sphere approximation (ASA) for the potential leads to errors in describing the electronic structure which are comparable to the absolute errors incurred by using the LSDA. The tight-binding linearized muffin tin orbital (TB-LMTO) surface Green function (SGF) method was developed to study the electronic structure of interfaces and other layered systems. When combined with the coherent-potential approximation (CPA), it allows the electronic structure, charge and spin densities of layered materials with substitutional disorder to be calculated self-consistently very efficiently [73]. MTOs satisfy our requirements of being able to treat complex electronic structures efficiently.

To combine the WFM method with muffin-tin orbitals, it turns out to be convenient to use the so-called "tail-cancellation" condition[7]

$$\sum_{R',l'm'} [P^{\alpha}_{Rl}(\varepsilon)\,\delta_{RR'}\delta_{ll'}\delta_{mm'} - S^{\alpha}_{Rlm;R'l'm'}]\,c^{\alpha}_{R'l'm'} = 0\,, \qquad (37)$$

in terms of potential functions $P^{\alpha}_{Rl}(\varepsilon)$ which characterize the AS potentials and the screened structure constant[8] matrix $S^{\alpha}_{Rlm;R'l'm'}$ whose range in real space depends on a set of screening parameters $\{\alpha_l\}$. The set of parameters which minimize the range of hopping is denoted $\alpha = \beta$. The equation analogous to Eq. (4) which we use to solve the scattering problem is then

$$-\boldsymbol{S}^{\beta}_{i,i-1}\boldsymbol{c}_{i-1} + (\boldsymbol{P}^{\beta}_{i,i}(\varepsilon) - \boldsymbol{S}^{\beta}_{i,i})\,\boldsymbol{c}_i - \boldsymbol{S}^{\beta}_{i,i+1}\boldsymbol{c}_{i+1} = 0\,. \qquad (38)$$

$\boldsymbol{c}_i$ is a $(l_{\max}+1)^2\,N \equiv M$ dimensional vector consisting of the coefficients of the i-th layer $c_{i,Rlm}$ with N atomic sites R and $(l_{\max}+1)^2$ orbitals lm per site. For systems which are periodic along the interface the matrices in (38) are labelled by $\boldsymbol{k}_{\|}$ and Rlm runs over the orbitals within the lateral (super)cell.

The transmission coefficients can be then used to calculate the Landauer–Büttiker (LB) conductance using Eq. (1).[9] For diffusive magnetoelectronic devices, this quantity is not suitable since calculating $R^{\mathrm{LB}} = 1/G^{\mathrm{LB}}$ results in a finite "interface" resistance, even for a fictitious interface between identical materials. Schep et al. [4] derived an expression for the resistance of interfaces embedded in a diffusive medium which takes into account the finiteness of the conductance of perfect leads:

$$R^{\mathrm{Schep}}_{\sigma}(A\,|\,B) = \frac{h}{e^2}\left[\frac{1}{\sum |t^{\sigma}_{mn}|^2} - \frac{1}{2}\left(\frac{1}{N^{\sigma}_A} + \frac{1}{N^{\sigma}_B}\right)\right], \qquad (39)$$

where the first term is the reciprocal of the LB conductance and N^{σ}_A and N^{σ}_B are the Sharvin conductances (all in units of e^2/h) of the materials A and B forming the interface, equal to the number of propagating modes in either material. Alternatively, Sharvin conductances can be expressed as the surface area of the projection of the Fermi surface in the transport direction [75].

[7] This equation is nothing other than the KKR equation in the ASA in which the kinetic energy in the interstitial region is taken to be zero and the volume of the interstitial region is made to vanish by replacing the muffin tin spheres with space-filling atomic spheres [74]. This choice leads to structure constants which are energy and scale independent, unlike the KKR structure constants. The potential function $P_l(\varepsilon)$ is simply related to the logarithmic derivative $D_l(\varepsilon)$ as $P_l(\varepsilon) = 2(2l+1)\,(D_l(\varepsilon)+l+1)/(D_l(\varepsilon)-l)$.

[8] The unscreened structure constant matrix $S^{\alpha=0}$ does not depend on the potential and is determined solely by the geometry of the lattice.

[9] Evaluation of Eq. (1) for layered structures involves integration over the two-dimensional (2D) Brillouin zone (BZ). For metallic structures, the sampling density needed to achieve convergence in the range of 1% typically corresponds to about 4000 points in the full 2D zone.

3.1 Ordered interfaces The non-trivial spin-dependence of the transmission and reflection of electrons at magnetic interfaces provides the key to understanding phenomena such as oscillatory exchange coupling, giant- and tunneling-magnetoresistance, spin transfer torque, spin-pumping and spin-injection [76]. For well-studied material combinations such as Co | Cu and Fe | Cr, modest spin-dependence of the interface transmission [4, 8, 77] of the order of 10–20% is sufficient to account for experimental observations [78].

However, the confrontation of theory and experiment just referred to is at best indirect and model-dependent. Even though the theory of transport in small structures is formulated in terms of transmission and reflection matrices [36], measuring interface transparencies directly has proven quite difficult [79]. To identify interfaces suitable for experimental study, we undertook [41] a systematic materials-specific study of the orientation dependence of the interface transmission between pairs of isostructural metals whose lattice constants match within a percent or so in the hope that it will prove possible to grow such interfaces epitaxially. In the following sections we will use the results of these calculations, summarized in Table 1, to discuss various mechanisms which control the scattering at interfaces.

Table 1 Sharvin conductances and interface transmissions in units of $10^{15}\ \Omega^{-1}\,\mathrm{m}^{-2}$, interface resistances R [4, 8] for ideal (and, in brackets, for disordered) interfaces in units of $10^{-15}\ \Omega\mathrm{m}^2$. Interface disorder was modeled in 10×10 lateral supercells with two layers of 50–50 alloy. The largest uncertainty between different configurations of disorder is at most 5%. The values given are for a single spin. For the pairs of materials and orientations indicated by a (*), comparison of the interface resistances shown in the last two columns with experimental values extracted from measurement on multilayers by the MSU group [78, 79] yields reasonable quantitative agreement [4, 8, 39].

$A \mid B$		G_A	G_B	$G_{A\mid B}$	R^{Schep}
Al | Ag	(111)	0.69	0.45	0.41 (0.36)	0.64 (0.92)
$a_{\mathrm{fcc}} = 4.05$ Å	(110)	0.68	0.47	0.30 (0.32)	1.60 (1.39)
	(001)	0.73	0.45	0.22 (0.24)	2.82 (2.37)
Al | Au	(111)	0.69	0.44	0.41 (0.35)	0.60 (0.99)
$a_{\mathrm{fcc}} = 4.05$ Å	(001)	0.73	0.46	0.24 (0.26)	2.37 (2.14)
Pd | Pt	(111)	0.62	0.71	0.55 (0.54)	0.30 (0.33)
$a_{\mathrm{fcc}} = 3.89$ Å	(001)	0.58	0.70	0.52 (0.51)	0.37 (0.39)
W | Mo	(001)	0.45	0.59	0.42 (0.42)	0.42 (0.42)
$a_{\mathrm{bcc}} = 3.16$ Å	(110)	0.40	0.54	0.37 (0.38)	0.52 (0.47)
Cu | Co	(111)*	0.56	0.47	0.43 (0.43)	0.34 (0.35)
majority	(001)	0.55	0.49	0.46 (0.45)	0.26 (0.27)
$a_{\mathrm{fcc}} = 3.61$ Å	(110)	0.59	0.50	0.46 (0.46)	0.35 (0.35)
Cu | Co	(111)*	0.56	1.05	0.36 (0.31)	1.38 (1.82)
minority	(001)	0.55	1.11	0.32 (0.32)	1.79 (1.79)
$a_{\mathrm{fcc}} = 3.61$ Å	(110)	0.59	1.04	0.31 (0.35)	1.89 (1.55)
Cr | Fe	(111)	0.61	0.82	0.27 (0.31)	2.22 (1.84)
majority	(001)	0.64	0.82	0.11 (0.25)	7.46 (2.55)
$a_{\mathrm{bcc}} = 2.87$ Å	(110)	0.59	0.78	0.22 (0.27)	3.04 (2.18)
Cr | Fe	(111)	0.61	0.41	0.34 (0.34)	0.93 (0.95)
minority	(001)	0.64	0.46	0.35 (0.35)	0.98 (0.95)
$a_{\mathrm{bcc}} = 2.87$ Å	(110)*	0.59	0.40	0.32 (0.32)	1.03 (1.06)

The Sharvin conductances, G_A and G_B, reported in the third and fourth columns of Table 1 are properties of the bulk materials and measure the current-carrying capacity of the conductor in the ballistic regime. Comparing these with the conductances $G_{A|B}$ [i.e. transmissions integrated over two-dimensional Brillouin zones] for non-magnetic Pd | Pt, W | Mo and for the high conductance Cu | Co (majority) and Cr | Fe (minority) channels, reveals the following trends: (i) $G_{A|B}$ tends to be slightly lower than the lesser of the two Sharvin conductances and (ii) the orientation dependence of $G_{A|B}$ is modest (at most ~15% for W | Mo) and mimics the behaviour of the lower Sharvin conductance. In all these cases the electronic structures of the respective materials are similar, i.e. the bands crossing the Fermi level are characterized by the same symmetries and orbital composition. In such situations the transmission tends to be high and the total conductance is determined largely by the geometrical overlap of the projected Fermi surfaces (FS).

3.1.1 Cu | Co: Majority spins The above can be illustrated straightforwardly for the Cu | Co interface. The majority-spin FS of each metal consists of a single nearly-free-electron like distorted sphere with necks developing in the vicinity of the 3D BZ boundary in the [111] directions. In Fig. 6 they are shown in projection along [001] and [011] directions. In the transport calculations we use 2D BZs defined by the in-plane translational symmetry. These are shown in the bottom corners of Fig. 6 as dashed lines overlaid on the projected 3D BZs. Folding of the original projected 3D FSs into the smaller 2D BZs yields Figs. 6a, b, d and e where the color scale denotes the number of states per $\boldsymbol{k}_{\parallel}$-point. Note that the green areas of the plots contain pairs of states originating from the same single-sheeted 3D FS.

The transmission probabilities shown in the two central panels of the bottom row of Fig. 6 as a function of $\boldsymbol{k}_{\parallel}$, the wave-vector parallel to the interface, follow a simple pattern. Wherever there exist states on both sides of the interface, the transmission is close to the upper theoretical limit of $\min(n_A, n_B)$ where $n_{A(B)}$ is the number of propagating states in material $A(B)$ at the given $\boldsymbol{k}_{\parallel}$.[10] Consequently the total, integrated transmission (conductance in e^2/h units) is well approximated simply by the area of the overlap of the projected FS. The transmission is additionally modulated by the velocity mismatch effect [80, 81], reminiscent of the free-electron formula for transmission through the potential step: $T = 4v_{\mathrm{L}}v_{\mathrm{R}}/(v_{\mathrm{L}} + v_{\mathrm{R}})^2$ where $v_{\mathrm{L/R}}$ are the components of the Fermi velocities in the transport direction. In most cases this effect is rather modest and becomes of importance only when a large difference of velocities exists

[10] In the absence of disorder $\boldsymbol{k}_{\parallel}$ is conserved.

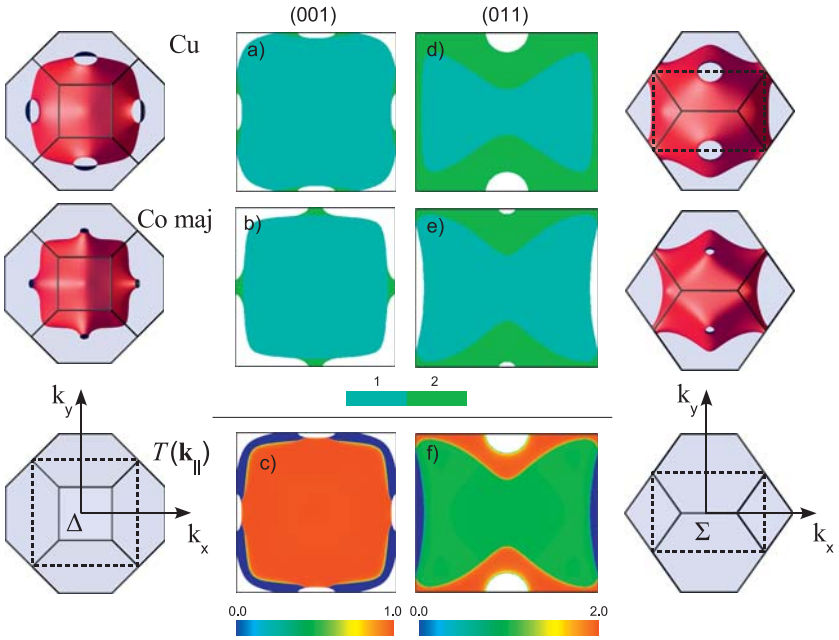

Figure 6 (online colour at: www.pss-b.com) Fermi surfaces of fcc Cu (top row) and majority spin Co (middle row) viewed along the [001] (left hand column) and [011] (right hand column) directions with a projection of the bulk fcc Brillouin zone onto a plane perpendicular to these directions (bottom row, solid lines); the 2D BZ for both orientations is shown (dashed lines) superimposed upon the projection of the bulk BZ. Central Panels: FS projections onto a plane perpendicular to the [001] (a, b) and [011] (d, e) directions folded into the 2D BZ. The number of propagating states is shown using the color bar; (bottom row) $\boldsymbol{k}_\parallel$-resolved transmission probabilities for majority-spin states, $T(\boldsymbol{k}_\parallel)$, for (001) and (011) oriented interfaces, respectively.

(thus "velocity mismatch"). This happens e.g. at the edges of the projected FS where $v_{L/R}$ drops to zero.

3.1.2 Cu | Co: Minority spins When the states on either side of the interface have different orbital character, *matrix element effects*, reducing the transmission between states possessing different symmetry and/or orbital composition, become the most prominent factor controlling the scattering. This is the case e.g. for minority spin electrons in the Cu | Co system where *sp* states in Cu encounter strongly *d*-hybridized states in Co. The relevant Fermi surfaces and their projections for (001) and (011) orientations are shown in Fig. 7. The open 3d shell of Co gives rise to a FS with multiple sheets and complex topology. The mismatch of the band states in Cu and Co results in a lowering of the total transmission by 15–30% depending on the orientation. Even though the net reduction is modest, the $\boldsymbol{k}_\parallel$-resolved transmissions shown in Fig. 7c and f reveal striking differences by comparison with the majority channel. Next to regions of high transmission, we now have areas of low or even vanishing transmission even for $\boldsymbol{k}_\parallel$-points where there are many states available in Co for

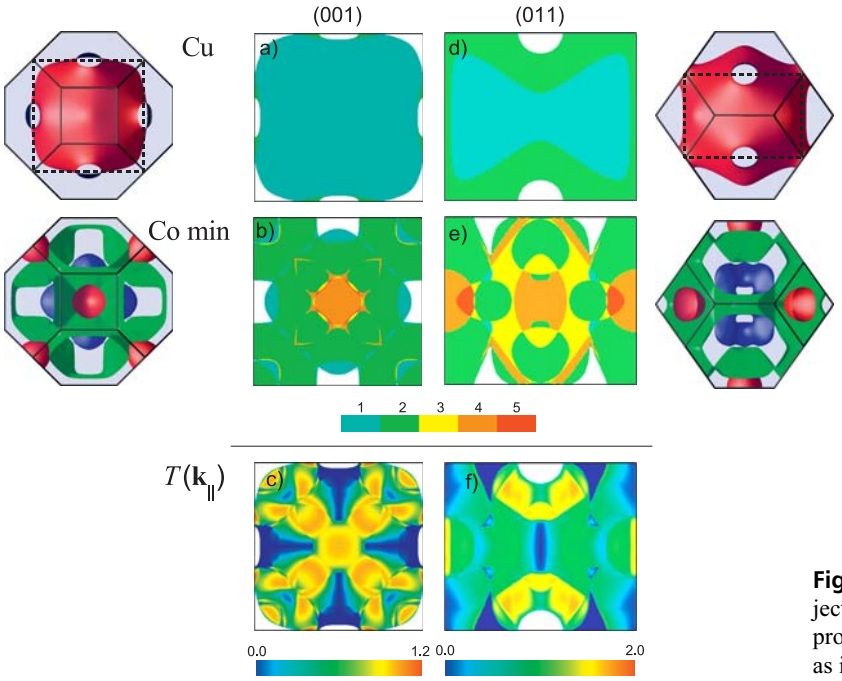

Figure 7 (online colour at: www.pss-b.com) Projected Fermi surfaces and $\boldsymbol{k}_\parallel$-resolved transmission probability for Cu | Co (001) and (011) interfaces as in Fig. 6 but for the minority spin electrons.

Cu states to scatter into. The intricate patterns of transmission can be interpreted in terms of the symmetries and orbital composition of Cu and Co states. For example, in the center of the 2D BZ for the (001) interface we have a single Δ_1 state in Cu composed predominantly of s and p_z orbitals. Facing it across the interface are four Co states: a doubly degenerate Δ_5 state consisting of p_x, p_y, d_{xz} and d_{yz} orbitals and two singly degenerate Δ_1 states.[11] The Δ_5 states are orthogonal to Δ_1 in Cu and consequently do not contribute to transmission. The scattering between symmetry-compatible Δ_1 states saturates the channel ($T = 0.99$). Whereas the axial symmetry of the Co Δ_1 states is identical they differ considerably in their orbital composition. One of them, similar to its Cu counterpart, consists predominantly of s- and p_z-orbitals and receives most of the transmission ($T = 0.95$). The other is dominated by $d_{3z^2-r^2}$ character and contributes little to the total transmission.

Once we move away from the center we encounter (going along the *y*-axis as defined in the bottom-left panel of Fig. 6) states which are either even or odd with respect to the *y,z*-plane. The states derived from the central Δ_1 modes in Cu and Co remain even. The Δ_5 ones split into solutions of even (p_y, d_{yz}) and odd (p_x, d_{xz}) symmetry. Initially, the transmission remains high and is provided mostly by scattering into states derived from "sp"-like Δ_1 and even $\Delta_5$states. Moving further from the center we reach a point where we encounter only odd states in Co and the transmission drops to zero.

Although symmetry selection rules like those discussed above are strictly only valid for symmetry points and lines in the 2D BZ, they can serve as a useful guide for understanding the situation close by.

3.1.3 Al | Ag Examination of the numbers given in Table 1 for Al | Ag (and Al | Au) reveals a surprising, factor 2 difference between the interface conductances for (111) and (001) orientations. The effect is insensitive to disorder (see the values in brackets) and does not correspond to the behaviour of the Sharvin conductance that exhibits only a very modest degree of orientation dependence. What make the effect surprising is not only its magnitude, unique among systems reported in Table 3.1,[12] but also the fact that it has been predicted for a remarkably simple system. Aluminium is a textbook [82] example of a system well described by the (nearly) free electron model. Silver, also usually assumed to be a free electron-like material, is a noble metal with high conductivity which is frequently used for electrical contacting. However, for truly free electrons the anisotropy should vanish.

The transmission probability for the (111) and (001) orientations is plotted in Fig. 8c and f within the 2D BZ. A

[11] The two Co Δ_1 states are degenerate in energy but differ in the values of the components of their wave vectors normal to the interface.

[12] Fe | Cr is an exception. For the majority spin channel, a large orientation dependence of the interface transmission is predicted. Unlike the Al | Ag case, this result is very sensitive to interface disorder. In addition, a single spin channel cannot be studied directly making it difficult to obtain an unambiguous experimental result.

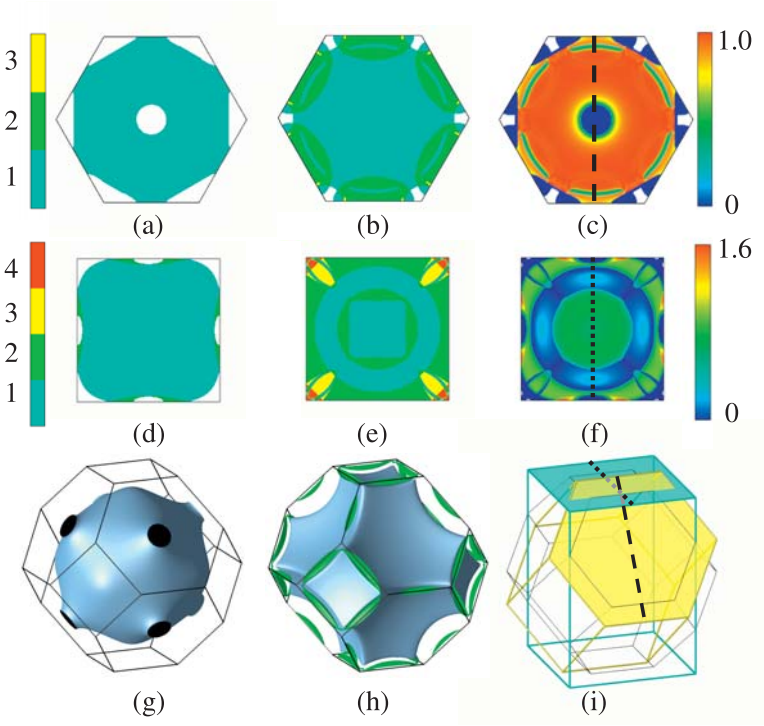

Figure 8 (online colour at: www.pss-b.com) Top row: Fermi surface projections for (a) Ag, (b) Al and (c) transmission probabilities in 2DBZ for (111) orientation. Middle row: Same for (001) orientation. The color bars on the left indicate the number of scattering states in the leads for a given two dimensional wave vector $\boldsymbol{k}_{\parallel}$. The transmission probabilities indicated by the color bars on the right can exceed 1 for $\boldsymbol{k}_{\parallel}$ s for which there is more than one scattering state in both Ag and Al. Bottom row: Fermi surfaces of (g) Ag and (h) Al, (i) the interface adapted BZ for (001) and (111) orientations. The vertical dashed line in (c) and on the yellow plane in panel (i) indicate the cross-section used in the left-hand panel of Fig. 9 while the vertical dotted line in (f) and on the blue plane in panel (i) indicate the cross-section used in the right-hand panel.

qualitative difference between the two orientations can be observed. In the (111) case, the transmission is almost uniformly high wherever there are states on both sides of the interface. The situation here is quite analogous to the previously discussed majority spin channel of Cu | Co. The (001) orientation exhibits more variation with high transmission in the central and outer regions of the 2D BZ but much lower in a ring-shaped region in between. The presence of this "cold ring" is the reason why the total transmission is lower for the (001) orientation. Explaining the transparency anisotropy of Al | Ag interfaces requires finding an explanation for the low transmission values in this region of the 2D BZ.

None of the mechanisms discussed previously can be responsible for the low values of transmission. Naive application of the free electron formula (i.e. velocity mismatch) yields uniformly good transmission[13] independent of the orientation. Examination of the eigenvectors demonstrates that the symmetry and orbital composition of the states in Al and Ag is the same. Therefore the reduction of the transmission can not be explained by the symmetry mismatch argument. The origin of the "cold ring" must be sought elsewhere.

In spite of the failure of the free electron transmission formula, the simple free electron model serves as a useful starting point for analyzing the Fermi surface (FS) topologies. In the simplest possible approach, we model the FS of Ag (shown in Fig. 8g) as a sphere which fits into the first BZ. A larger sphere, accommodating three electrons, is needed for trivalent Al. In an extended BZ scheme, conservation of momentum parallel to the interface dictates that the transmission through a specular interface is nonzero only between states with the same values of $\boldsymbol{k}_{\|}$; these are the $\boldsymbol{k}_{\|}$-vectors belonging to the region where projections of the Fermi spheres on a plane perpendicular to the transport direction overlap. For systems with lattice periodicity, we must use a downfolded FS, with fragments of the original FS sphere back-translated into the 1st Brillouin zone, a procedure which can be realized geometrically by placing spheres accommodating three electrons on reciprocal lattice (RL) sites and then only considering the fragments in the first BZ. Examination of the FS of Al calculated from first-principles (Fig. 8h) and its cross-section (Fig. 9) reveals that, in spite of its apparent complexity, it remains essentially (piecewise) spherical. For some values of $\boldsymbol{k}_{\|}$ (see Fig. 8b and e), Al can now have more than one propagating state. Nevertheless, in the free electron limit, the downfolded states are strictly orthogonal to the states in Ag and the total transmission is unchanged. For a reduced zone scheme, we formulate the following rule: *The transmission between states in two (nearly) free electron materials which have the same $\boldsymbol{k}_{\|}$, but originate from reciprocal lattice sites whose parallel components do not coincide, vanishes in the free electron limit and is expected to be strongly suppressed for nearly free electron like materials.*

Obviously, the truly free electron system can not exhibit anisotropy. However, in the presence of the periodic potential the original, piecewise-spherical Fermi surface and consequently the transmission is going to be modified. In Fig. 9, we show the intersection of the Al FS with a (110) plane. The two plots are rotated so that the vertical axis in Fig. 9a is the [111] direction while in Fig. 9b it is [001]. In both cases the positions of the nearest RL sites (on which spheres are centered) are shown together with the cross-section through the relevant interface-adapted Brillouin zone, which is different for each orientation; see Fig. 8i. We can now readily identify spheres from which various fragments of the Fermi surface originate and mark those fragments with positive (upward) velocities, according to the rule given above, as having high (red) or low (blue) transmissions. In the (001) case, the "high" fragments originate from (0, 0, 0) and (0, 0, –2) centered spheres. Comparing Figs. 8f and 9b, we note that the position of the gaps opened between these spheres by Bragg reflection on the (001) and (00 $\bar{1}$) planes coincides, in projection along the [001] direction, with the position of the

[13] Moreover the free electron formula would lead to the violation of the unitarity of the scattering matrix (i.e. the conservation of particles) whenever there is more than one state on either side of the interface.

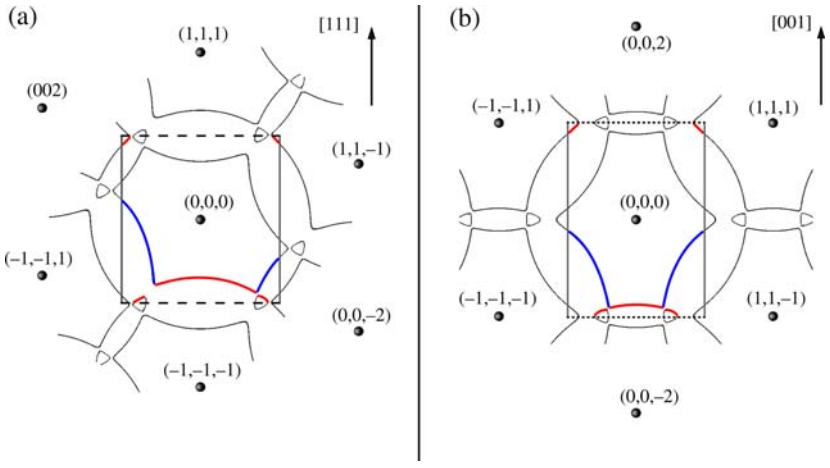

Figure 9 (online colour at: www.pss-b.com) Intersection of a (110) plane with the Al Fermi surface and with the interface adapted BZs indicated in Fig. 8i (where the meaning of the dashed and dotted lines is explained). The labeled dots indicate the positions of the RL sites with coordinates given in units of $2\pi/a$. The red (blue) lines indicate regions of high (low) transmission.

"cold ring" in Fig. 8f. The other states present in this region originate from (–1, –1, –1) (and equivalent) centered spheres, are therefore nearly orthogonal to states in Ag centered on (0, 0, 0) and so have low transmission. In the (111) case however, the large fragments of FS belonging to the same (–1, –1, –1) sphere have high transmissions (Fig. 9a) and dominate transport. In addition, the effect of gap-opening is reduced in this orientation because of the rotation. Combination of these two factors results in the almost uniformly high transmission seen in Fig. 8c.

Finally, we can identify the origin of the transmission anisotropy for Al|Ag interface. It stems from two factors: (i) the near orthogonality of the downfolded Al states to those belonging to the simple Ag sphere and (ii) the gaps opened in the continuous free electron Fermi surface by the periodic potential. The latter factor is of course related to the symmetry of the underlying crystal lattice and directly responsible for the introduction of the orientation dependence. For Al | Au interfaces, the interface transmissions and resistances are very similar to the Al | Ag case. The predicted anisotropic interface resistance and Andreev reflection (not shown) are not very sensitive to interface disorder and should be observable experimentally.

A free electron description of interface scattering, in which the effect of the crystal potential on transport is completely neglected, underlies the Blonder–Tinkham–Klapwijk or BTK theory [83] used to interpret [80, 81] Andreev reflection (AR) experiments. Point contact AR experiments are increasingly used to identify the pairing symmetry of superconductors and, in the field of magnetoelectronics, to determine the polarization of magnetic materials [84, 85]. Our finding that the electronic structure can have such a large effect on the interface transmission, implies that experiments should be analyzed using more sophisticated models.

3.1.4 Ordered interfaces: Summary Interface scattering between the band states is a complex process, especially in the presence of open 3d shells of ferromagnetic transition metals, which does not easily lend itself to a description in terms of simple models. However, using the examples discussed in the previous sections, we can identify the following mechanisms influencing the transmission through specular ($\boldsymbol{k}_{\parallel}$-preserving) interfaces:

– *velocity mismatch*: reminiscent of the free electron formula and effective only for substantial differences between the Fermi velocities of the states, e.g. when one of the states is located close to the border of the FS projection where the velocity in the transport direction vanishes,

– *orthogonality between different sheets of nearly free-electron Fermi surface*: as discussed in 3.1.3 for Al | Ag,

– *geometry of the Fermi surface*: relating the LB interface conductance to the area of overlap of the projected FSs,

– *matrix element effects*: the effect of symmetry and orbital composition, reducing the transmission between mismatched states.

Another important source of interface scattering is the disorder present to some extent in all experimental systems, to be discussed in the following section.

3.2 Interface disorder Instructive though the study of perfect interfaces may be in providing an understanding of the role electronic structure mismatch may play in determining giant magnetoresistive effects, all measurements are made on devices which contain disorder, in the diffusive regime. The TB-MTO scheme is computationally very efficient and allows us to use large lateral supercells to model in a simple fashion interface disorder, interfaces between materials whose underlying lattices are incommensurate, or quantum point contacts. This treatment becomes formally exact in the limit of infinitely large supercells. In practice, satisfactory convergence is achieved for supercells of quite moderate size. For disordered metallic interfaces the convergence is typically in the range of 3–5% for 10×10 supercells and reduces to 1% for 20×20 cells.

To perform fully self-consistent calculations for a number of large lateral supercells and for different configurations of disorder would be prohibitively expensive. Fortunately, the coherent potential approximation (CPA) is a very efficient way of calculating charge and spin densities for a substitutional disordered A_xB_{1-x} alloy with an expense comparable to that required for an ordered system with a minimal unit cell [86]. The output from such a calculation are atomic sphere potentials for the two sites, υ_A and υ_B. The layer CPA approximation generalizes this to allow the concentration to vary from one layer to the next [73]. Once υ_A and υ_B have been calculated for some concentration x, an $N \times N$ lateral supercell is constructed in which the potentials are distributed at random, maintaining the concentration for which they were calculated self-consistently. A full discussion of technical details is given in [39].

Figure 10 shows the interface resistance of a Cu | Co (111) interface calculated for three models of substitutional disorder (also shown in the figure). The values are plotted as a function of x and compared with a range of experimental values from the literature. Comparing the resistances without and with disorder, we see that disorder has virtually no effect on the majority spin channel which is a consequence of the great similarity of the Cu and Co majority spin potentials and electronic structures. The transmission remains almost entirely specular,[14] that is the scattering occurs only between states with the same parallel component of the wave vector, $\boldsymbol{k}_{\parallel}$.

[14] Equation (39) used to calculate resistances in Fig. 10 assumes a lack of coherent scattering between subsequent interfaces. This assumption is most likely not valid for the Cu | Co majority spin channel. Including coherent scattering, using multilayer calculations, leads to interface resistances substantially lower than values derived from experiment. See [39] for a fuller discussion.

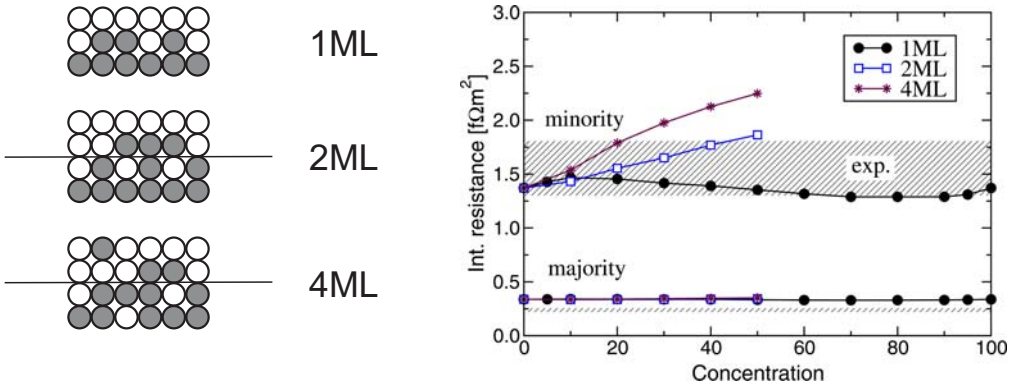

Figure 10 (online colour at: www.pss-b.com) Left panel: Illustration of 3 different models of interface disorder considered. Top (1ML): disorder is modeled using one monolayer (ML) of $[Cu_{1-x}Co_x]$ alloy between Cu and Co leads, denoted as $Cu[Cu_{1-x}Co_x]Co$. Middle (2ML): disorder modeled in two MLs as $Cu[Cu_{1-x}Co_x \mid Cu_xCo_{1-x}]Co$. Bottom (4ML): starting from the 2ML disorder case, 1/3 of the concentration x of impurity atoms is transferred to the next layer resulting in disorder in four MLs: $Cu[Cu_{1-(x/3)}Co_{x/3} \mid Cu_{1-(2x/3)}Co_{2x/3} \mid Cu_{2x/3}Co_{1-(2x/3)} \mid Cu_{x/3}Co_{1-(x/3)}]Co$. Right panel: Interface resistance for disordered interfaces as a function of the alloy concentration used to model disordered interfaces, calculated using (39). The experimental values for sputtered and MBE grown multilayers cited in Table 1 of [78] span a range of values which is indicated by the shaded regions.

In the minority-spin channel the effect of disorder is much more pronounced. Even for the 1ML model, where the total interface resistance exhibits only weak modulation, the disorder is strong enough to change the character of transmission. In the range $x = 0.2$ to 0.8, transport is dominated by diffusive scattering whereby the $\boldsymbol{k}_{\parallel}$ values are changed. For the more strongly disordered 2ML and 4ML models, transport is also dominated by diffuse processes and the variation of the resistance is greater. Two MLs of 50% alloy ($x = 0.5$) are sufficient to essentially wash away all the symmetry effects discussed in section 3.1.2. For all incoming states in Cu the total transmission, summed over all outgoing states in Co, becomes comparable [39].

The results for other interfaces are given in Table 1 for the 2ML ($x = 0.5$) model. Of particular interest is the Cr | Fe (001) system. The low-resistance minority channel is – like the Cu | Co majority spin case – hardly influenced by disorder. In the high-resistance majority channel however we observe a factor 3 *reduction* of the interface resistance. It is worth noting that the conductance for the original, perfect interface is exceptionally low and reaches only about 15% of the Cr Sharvin conductance. This reflects the poor matching of the electronic structures of the two metals [8, 87]. The diffuse scattering introduced by disorder opens new channels for transmission and increases the transparency of the interface thus reducing the interface resistance.

The effect of disorder on transmission is highly material specific but rules of thumb can be formulated for the two extreme cases: (i) the conductance of interfaces between materials with almost perfectly matched states (e.g. Cu | Co majority) is not hugely sensitive to disorder; (ii) the transmission between sets of poorly matched states (e.g. differing in symmetry) tends to be increased by disorder.

3.3 Spin-injection, spin-tunneling Spin-dependent matching of electronic structures does not only play a role at interfaces between metallic ferromagnets and nonmagnetic metals. It also occurs at the interface between itinerant ferromagnets and semiconductors or insulators where the electronic structure of the semiconductor/insulator in a very small region of reciprocal space dominates the injection/tunneling. This happens when there is lattice matching and in the absence of disorder so transverse crystal momentum is conserved. Most work has focused on systems containing Fe(001)-related interfaces because in this orientation the lattice constant of Fe is reasonably well matched to those of a number of inorganic semiconductors and to MgO. The electronic structures were either calculated directly from first-principles [27, 45, 88–96] or obtained by fitting to first-principles electronic structures [23, 25, 28, 29, 97].

Unlike metallic systems, the current in semiconductors or tunnel junctions is carried by a very small number of channels. In zinc-blende semiconductors these are concentrated around the center of the BZ and possess (along [001]) Δ_1^{zb} symmetry. Focusing on the Fe | InAs (001) system as a typical example, we observe a very high polarization for an ordered interface (Fig. 11). This is the result of good matching between the Δ_1 states present at the Fermi energy in the majority band structure of Fe to the conduction band states in InAs. The Fe minority spin states are nearly orthogonal to Δ_1^{zb} and are almost completely reflected at the interface.[15] In the presence of disorder the system follows the general rule sketched in the previous

[15] The same symmetry considerations also hold for Fe | GaAs and Fe | ZnSe (001) [94].

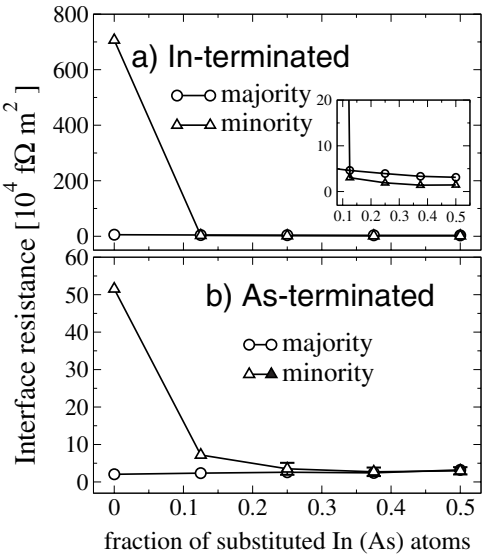

Figure 11 Interface resistances of InAs | Fe for a) In- and b) As-termination as a function of the fraction of interfacial In or As atoms substituted by Fe for majority (○) and minority (△) spins. For both terminations the symmetry-induced spin-asymmetry is strongly reduced by disorder.

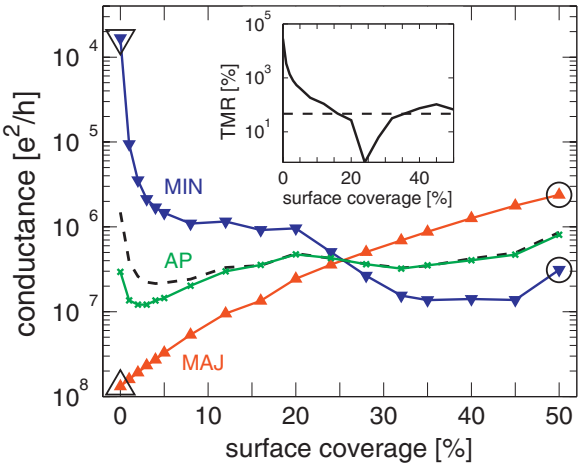

Figure 12 (online colour at: www.pss-b.com) Configuration-averaged conductances $G_P^{\min}$ (▼), G_P^{maj} (▲), and G_{AP}^{σ} (×) of an Fe | vacuum | Fe magnetic tunnel junction with 8 ML thick vacuum barrier as a function of the surface coverage, normalized to a 1×1 surface unit cell. The dashed line denotes $G_{AP}^{\sigma} = \sqrt{G_P^{\mathrm{maj}} G_P^{\min}}$. Inset: TMR as a function of the surface coverage. The dashed line is the value predicted using Julliere's expression and a calculated DOS polarization of 55%.

section. The well-matched majority channel is only weakly influenced by disorder. In the poorly-matched minority channel on the other hand we observe a massive increase of the transmission (and reduction of the interface resistance) occurring via diffuse scattering. The net result is a rapid quenching of the original very high polarization [45].

Extremely high polarization of the tunneling currents was predicted also for disorder-free tunnel junctions [27, 28]. So far, only much lower values have been measured, including the recent experiments on single-crystal MgO-based tunnel junctions [98–100]. In Fig. 12 we show the effect of disorder, in the form of surface roughness, on the tunneling in a model Fe | vacuum | Fe junction. Transport for an ideal system (0% coverage) is dominated by resonant tunneling in the minority channel, the effect associated with the presence of a Δ_1 surface state on the Fe surface [101]. In the presence of disorder the resonant channels are removed. The minority conductance decreases and eventually drops below the majority channel values.[16] Interestingly for all but the cleanest interfaces the conductance of the antiparallel configuration follows the simple formula: $G_{AP}^{\sigma} = \sqrt{G_P^{\mathrm{maj}} G_P^{\min}}$. This suggest that the tunneling conductance through a general non-symmetric junction (with enough disorder to remove resonant channels) can be expressed in a factorized form reminiscent of a Julliere formula [102].

The polarization of both injected and tunneling current depends sensitively on the detailed interface structure. While the quality of tunnel junctions is clearly improving, much more work needs to be done to characterize the experimental disorder quantitatively.

4 Outlook So far we have been concerned with the quantitative and qualitative characteristics of the transmission and reflection of electron states at *single* interfaces between real materials, one of which is an itinerant ferromagnet. The advantage of focusing on the full scattering matrix, rather than simply calculating the conductance, is that it provides us with greater insight and is a very convenient point of contact with other theories, such as random matrix theory [36] or circuit theory [37]. By interfacing with phenomenological theories, we can make contact relatively easily with more complex transport problems. A good example of this is the study of the materials dependence of the suppression of Andreev scattering at a ferromagnetic | superconducting interface. This is a problem which had been studied phenomenologically [36] without taking into account details of the electronic structure of materials which might be used in an actual experiment. Because it had been formulated in terms of the scattering matrix for the F | S interface with the superconducting material in its normal state, it was straightforward to introduce and study the dependence on the constituent materials [44]. We argue that such an approach may be more fruitful than a frontal, brute force approach to calculating transport properties entirely from first principles.

Acknowledgements This work is supported by "NanoNed", a nanotechnology programme of the Dutch Ministry

[16] The increase of the majority conductance is related to the specific model considered here. Increasing the coverage of the Fe electrodes decreases the average distance between them and promotes the tunneling.

of Economic Affairs. It is part of the research programs of "Chemische Wetenschappen" (CW) and "Stichting voor Fundamenteel Onderzoek der Materie" (FOM) and the use of supercomputer facilities was sponsored by the "Stichting Nationale Computer Faciliteiten" (NCF), all financially supported by the "Nederlandse Organisatie voor Wetenschappelijk Onderzoek" (NWO). MZ wishes to acknowledge support from EU grant CARDEQ under contract IST-021285-2. KX is financially supported by NSF (grant 10634070) and MOST (grants 2006CB933000 and 2006AA03Z402) of China.

References

[1] M. D. Stiles and D. R. Hamann, Phys. Rev. B **38**, 2021 (1988).
[2] M. D. Stiles and D. R. Hamann, Phys. Rev. Lett. **66**, 3179 (1991).
[3] N. D. Lang, Phys. Rev. B **52**, 5335 (1995).
[4] K. M. Schep, J. B. A. N. van Hoof, P. J. Kelly, G. E. W. Bauer, and J. E. Inglesfield, Phys. Rev. B **56**, 10805 (1997).
[5] J. B. A. N. van Hoof, K. M. Schep, A. Brataas, G. E. W. Bauer, and P. J. Kelly, Phys. Rev. B **59**, 138 (1999).
[6] J. M. MacLaren, X.-G. Zhang, W. H. Butler, and X. Wang, Phys. Rev. B **59**, 5470 (1999).
[7] J. Kudrnovský, V. Drchal, C. Blaas, P. Weinberger, I. Turek, and P. Bruno, Phys. Rev. B **62**, 15084 (2000).
[8] K. Xia, P. J. Kelly, G. E. W. Bauer, I. Turek, J. Kudrnovský, and V. Drchal, Phys. Rev. B **63**, 064407 (2001).
[9] I. Riedel, P. Zahn, and I. Mertig, Phys. Rev. B **63**, 195403 (2001).
[10] J. Taylor, H. Guo, and J. Wang, Phys. Rev. B **63**, 245407 (2001).
[11] M. Brandbyge, J.-L. Mozos, P. Ordejón, J. Taylor, and K. Stokbro, Phys. Rev. B **65**, 165401 (2002).
[12] J. J. Palacios, A. J. Pérez-Jiménez, E. Louis, E. SanFabián, and J. A. Vergés, Phys. Rev. B **66**, 035322 (2002).
[13] D. Wortmann, H. Ishida, and S. Blügel, Phys. Rev. B **65**, 165103 (2002).
[14] D. Wortmann, H. Ishida, and S. Blügel, Phys. Rev. B **66**, 075113 (2002).
[15] K. S. Thygesen, M. V. Bollinger, and K. W. Jacobsen, Phys. Rev. B **67**, 115404 (2003).
[16] P. Mavropoulos, N. Papanikolaou, and P. Dederichs, Phys. Rev. B **69**, 125104 (2004).
[17] P. A. Khomyakov and G. Brocks, Phys. Rev. B **70**, 195402 (2004).
[18] S. V. Faleev, F. Léonard, D. A. Stewart, and M. van Schilfgaarde, Phys. Rev. B **71**, 195422 (2005).
[19] A. R. Rocha, V. Garcia-Suarez, S. W. Bailey, C. J. Lambert, J. Ferrer, and S. Sanvito, Phys. Rev. B **73**, 85414 (2006).
[20] Z. Y. Li and D. S. Kosov, J. Phys.: Condens. Matter **18**, 1347 (2006).
[21] P. Havu, V. Havu, M. J. Puska, M. H. Hakala, A. S. Foster, and R. M. Nieminen, J. Chem. Phys. **124**, 054707 (2006).
[22] A. Bagrets, N. Papanikolaou, and I. Mertig, Phys. Rev. B **75**, 235448 (2007).
[23] E. Y. Tsymbal and D. G. Pettifor, J. Phys.: Condens. Matter **9**, L411 (1997).
[24] J. Mathon, Phys. Rev. B **55**, 960 (1997).
[25] J. Mathon, Phys. Rev. B **56**, 11810 (1997).
[26] S. Sanvito, C. J. Lambert, J. H. Jefferson, and A. M. Bratkovsky, Phys. Rev. B **59**, 11936 (1999).
[27] W. H. Butler, X. G. Zhang, T. C. Schulthess, and J. M. MacLaren, Phys. Rev. B **63**, 054416 (2001).
[28] J. Mathon and A. Umerski, Phys. Rev. B **63**, 220403(R) (2001).
[29] J. Mathon and A. Umerski, Phys. Rev. B **71**, 220402 (2005).
[30] C. Caroli, R. Combescot, P. Nozières, and D. Saint-James, J. Phys. C, Solid State Phys. **4**, 916 (1971).
[31] D. S. Fisher and P. A. Lee, Phys. Rev. B **23**, 6851 (1981).
[32] P. A. Khomyakov, G. Brocks, V. Karpan, M. Zwierzycki, and P. J. Kelly, Phys. Rev. B **72**, 035450 (2005).
[33] T. Ando, Phys. Rev. B **44**, 8017 (1991).
[34] J. E. Inglesfield, J. Phys. C, Solid State Phys. **14**, 3795 (1981).
[35] S. Crampin, J. B. A. N. van Hoof, M. Nekovee, and J. E. Inglesfield, J. Phys.: Condens. Matter **4**, 1475 (1992).
[36] C. W. J. Beenakker, Rev. Mod. Phys. **69**, 731 (1997).
[37] A. Brataas, G. E. W. Bauer, and P. J. Kelly, Phys. Rep. **427**, 157 (2006).
[38] P. A. Khomyakov and G. Brocks, Phys. Rev. B **74**, 165416 (2006).
[39] K. Xia, M. Zwierzycki, M. Talanana, P. J. Kelly, and G. E. W. Bauer, Phys. Rev. B **73**, 064420 (2006).
[40] O. K. Andersen, Z. Pawlowska, and O. Jepsen, Phys. Rev. B **34**, 5253 (1986).
[41] P. X. Xu, K. Xia, M. Zwierzycki, M. Talanana, and P. J. Kelly, Phys. Rev. Lett. **96**, 176602 (2006).
[42] K. Xia, P. J. Kelly, G. E. W. Bauer, A. Brataas, and I. Turek, Phys. Rev. B **65**, 220401 (2002).
[43] M. Zwierzycki, Y. Tserkovnyak, P. J. Kelly, A. Brataas, and G. E. W. Bauer, Phys. Rev. B **71**, 064420 (2005).
[44] K. Xia, P. J. Kelly, G. E. W. Bauer, and I. Turek, Phys. Rev. Lett. **89**, 166603 (2002).
[45] M. Zwierzycki, K. Xia, P. J. Kelly, G. E. W. Bauer, and I. Turek, Phys. Rev. B **67**, 092401 (2003).
[46] G. E. W. Bauer, A. Brataas, Y. Tserkovnyak, B. I. Halperin, M. Zwierzycki, and P. J. Kelly, Phys. Rev. Lett. **92**, 126601 (2004).
[47] G. E. W. Bauer, Y. Tserkovnyak, A. Brataas, J. Ren, K. Xia, M. Zwierzycki, and P. J. Kelly, Phys. Rev. B **72**, 155304 (2005).
[48] P. X. Xu, V. M. Karpan, K. Xia, M. Zwierzycki, I. Marushchenko, and P. J. Kelly, Phys. Rev. B **73**, 180402(R) (2006).
[49] M. Hatami, G. E. W. Bauer, Q. F. Zhang, and P. J. Kelly, Phys. Rev. Lett. **99**, 066603 (2007).
[50] S. Datta, Electronic Transport in Mesoscopic Systems (Cambridge University Press, Cambridge, 1995).
[51] J. R. Chelikowsky, N. Troullier, and Y. Saad, Phys. Rev. Lett. **72**, 1240 (1994).
[52] J. R. Chelikowsky, N. Troullier, K. Wu, and Y. Saad, Phys. Rev. B **50**, 11355 (1994).
[53] T. Ono and K. Hirose, Phys. Rev. B **82**, 5016 (1999).
[54] Y. Fujimoto and K. Hirose, Phys. Rev. B **67**, 195315 (2003).
[55] A. I. Yanson, G. Rubio-Bollinger, H. E. van den Brom, N. Agraït, and J. M. van Ruitenbeek, Nature **395**, 783 (1998).

[56] H. Ohnishi, Y. Kondo, and K. Takayanagi, Nature **395**, 780 (1998).
[57] N. Agraït, A. L. Yeyati, and J. M. van Ruitenbeek, Phys. Rep. **377**, 81 (2003).
[58] J. M. Krans, J. M. van Ruitenbeek, V. V. Fisun, I. K. Yanson, and L. J. Jongh, Nature **375**, 767 (1995).
[59] A. Yazdani, D. M. Eigler, and N. D. Lang, Science **272**, 1921 (1996).
[60] F. Yamaguchi, T. Yamada, and Y. Yamamoto, Solid State Commun. **102**, 779 (1997).
[61] N. D. Lang, Phys. Rev. Lett. **79**, 1357 (1997).
[62] H.-W. Lee and C. S. Kim, Phys. Rev. B **63**, 075306 (2001).
[63] J. Kübler, Theory of Itinerant Electron Magnetism (Oxford University Press, Oxford, 2002).
[64] P. Bruno, J. Magn. Magn. Mater. **121**, 248 (1993).
[65] M. D. Stiles, Phys. Rev. B **48**, 7238 (1993).
[66] M. D. Stiles, J. Appl. Phys. **79**, 5805 (1996).
[67] S. F. Zhang and P. M. Levy, J. Appl. Phys. **69**, 4786 (1991).
[68] S. F. Lee, W. Pratt Jr., Q. Yang, P. Holody, R. Loloee, P. A. Schroeder, and J. Bass, J. Magn. Magn. Mater. **118**, L1 (1993).
[69] J. B. A. N. van Hoof, Ph.D. thesis, University of Nijmegen, Nijmegen, The Netherlands (1997).
[70] J. B. A. N. van Hoof, K. M. Schep, P. J. Kelly, and G. E. W. Bauer, J. Magn. Magn. Mater. **177–181**, 188 (1998).
[71] O. K. Andersen and O. Jepsen, Phys. Rev. Lett. **53**, 2571 (1984).
[72] O. K. Andersen, O. Jepsen, and D. Glötzel, in: Highlights of Condensed Matter Theory, edited by F. Bassani, F. Fumi, and M. P. Tosi, International School of Physics 'Enrico Fermi', Varenna, Italy (North-Holland, Amsterdam, 1985), pp. 59–176.
[73] I. Turek, V. Drchal, J. Kudrnovský, M. Šob, and P. Weinberger, Electronic Structure of Disordered Alloys, Surfaces and Interfaces (Kluwer, Boston–London–Dordrecht, 1997).
[74] O. K. Andersen, Phys. Rev. B **12**, 3060 (1975).
[75] K. M. Schep, P. J. Kelly, and G. E. W. Bauer, Phys. Rev. B **57**, 8907 (1998).
[76] see the collection of articles, in Ultrathin Magnetic Structures I–IV, edited by J. A. C. Bland and B. Heinrich (Springer-Verlag, Berlin, 1994–2005).
[77] M. D. Stiles and D. R. Penn, Phys. Rev. B **61**, 3200 (2000).
[78] J. Bass and W. P. Pratt Jr., J. Magn. Magn. Mater. **200**, 274 (1999).
[79] C. Galinon, K. Tewolde, R. Loloee, W. C. Chiang, S. Olson, H. Kurt, W. P. Pratt Jr., J. Bass, P. X. Xu, K. Xia, and M. Talanana, Appl. Phys. Lett. **86**, 182502 (2005).
[80] I. I. Mazin, Phys. Rev. Lett. **83**, 1427 (1999).
[81] I. I. Mazin, A. A. Golubov, and B. Nadgorny, J. Appl. Phys. **89**, 7576 (2001).
[82] N. W. Ashcroft and N. D. Mermin, Solid State Physics (Holt-Saunders International Editions, Philadelphia, 1976).
[83] G. E. Blonder, M. Tinkham, and T. M. Klapwijk, Phys. Rev. B **25**, 4515 (1982).
[84] R. J. Soulen Jr., J. M. Byers, M. S. Osofsky, B. Nadgorny, T. Ambrose, S. F. Cheng, P. R. Broussard, C. T. Tanaka, J. Nowak, J. S. Moodera, et al., Science **282**, 85 (1998).
[85] S. K. Upadhyay, A. Palanisami, R. N. Louie, and R. A. Buhrman, Phys. Rev. Lett. **81**, 3247 (1998).
[86] P. Soven, Phys. Rev. **156**, 809 (1967).
[87] M. Talanana, Ph.D. thesis, University of Twente (2006).
[88] J. M. MacLaren, X.-G. Zhang, and W. H. Butler, Phys. Rev. B **56**, 11827 (1997).
[89] J. M. MacLaren, W. H. Butler, and X.-G. Zhang, J. Appl. Phys. **83**, 6521 (1998).
[90] H. C. Herper, P. Weinberger, A. Vernes, L. Szunyogh, and C. Sommers, Phys. Rev. B **64**, 184442 (2001).
[91] O. Wunnicke, P. Mavropoulos, R. Zeller, P. H. Dederichs, and D. Grundler, Phys. Rev. B **65**, 241306 (2002).
[92] P. Mavropoulos, O. Wunnicke, and P. Dederichs, Phys. Rev. B **66**, 024416 (2004).
[93] P. Weinberger, Phys. Rep. **377**, 281 (2003).
[94] O. Wunnicke, P. Mavropoulos, R. Zeller, and P. H. Dederichs, J. Phys.: Condens. Matter **16**, 4643 (2004).
[95] O. Bengone, O. Eriksson, J. Fransson, I. Turek, J. Kudrnovský, and V. Drchal, Phys. Rev. B **70**, 035302 (2004).
[96] X. G. Zhang and W. H. Butler, Phys. Rev. B **70**, 172407 (2004).
[97] J. Mathon and A. Umerski, Phys. Rev. B **60**, 1117 (1999).
[98] S. Yuasa, T. Nagahama, A. Fukushima, Y. Suzuki, and K. Ando, Nature Mater. **3**, 868 (2004).
[99] S. S. P. Parkin, C. Kaiser, A. Panchula, P. M. Rice, B. Hughes, M. Samant, and S. H. Yang, Nature Mater. **3**, 862 (2004).
[100] S. Yuasa, A. Fukushima, H. Kubota, Y. Suzuki, and K. Ando, Appl. Phys. Lett. **89**, 042505 (2006).
[101] O. Wunnicke, N. Papanikolaou, R. Zeller, P. H. Dederichs, V. Drchal, and J. Kudrnovský, Phys. Rev. B **65**, 064425 (2002).
[102] M. Julliere, Phys. Lett. A **54**, 225 (1975).

